



Core–mantle boundary topography as a possible constraint on lower mantle chemistry and dynamics

Teresa Mae Lassak^{a,*}, Allen K. McNamara^a, Edward J. Garnero^a, Shijie Zhong^b

^a School of Earth and Space Exploration, Arizona State University, Tempe, AZ 85287-1404, USA

^b Department of Physics, University of Colorado, Boulder, CO 80309-0390, USA

ARTICLE INFO

Article history:

Received 2 June 2009

Received in revised form 15 October 2009

Accepted 4 November 2009

Available online 27 November 2009

Editor: Y. Ricard

Keywords:

mantle convection
core–mantle boundary
CMB topography
thermochemical piles
plume clusters

ABSTRACT

The origin of large low shear-wave velocity provinces (LLSVPs) in the lowermost mantle beneath the central Pacific and Africa is not well constrained. We explore numerical convection calculations for two proposed hypotheses for these anomalies, namely, thermal upwellings (e.g., plume clusters) and large intrinsically dense piles of mantle material (e.g., thermochemical piles), each of which uniquely affects the topography on Earth's core–mantle boundary (CMB). The thermochemical pile models predict a relatively flat but elevated CMB beneath piles (presumed LLSVPs), with strong upwarping along LLSVP margins. The plume cluster models predict CMB upwarping beneath upwellings that are less geographically organized. Both models display CMB depressions beneath subduction related downwelling. While each of the two models produces a unique, characteristic style of CMB topography, we find that seismic models will require shorter length scales than are currently being employed in order to distinguish between the end-member dynamic models presented here.

© 2009 Elsevier B.V. All rights reserved.

1. Introduction

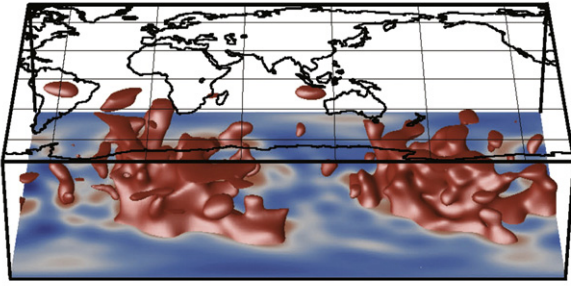
Geochemical evidence suggests the presence of chemically distinct reservoirs at depth in Earth's mantle that provide the source for ocean island basalts (OIB) and mid-ocean ridge basalts (MORB) (e.g., Hofmann, 1997). Seismic tomography offers evidence for two distinct, large, low shear-velocity provinces (LLSVPs) in the lowermost mantle beneath Africa and the central Pacific (Fig. 1A) (e.g., Dziewonski, 1984; Su et al., 1994; Grand et al., 1997; Su and Dziewonski, 1997; Ritsema et al., 1999; Mégnin and Romanowicz, 2000; Ritsema et al., 2004) in the Earth's lower mantle. These provinces display lower than average shear-wave velocities and are commonly interpreted to be hotter than the surrounding mantle. However, recent seismic waveform studies suggest that LLSVPs are chemically distinct from the surrounding mantle (Ni et al., 2002; Ni and Helmberger, 2003a,b; Wang and Wen, 2004; To et al., 2005; Ford et al., 2006) and global inversions argue that LLSVPs possess elevated density (e.g., Ishii and Tromp, 1999; Masters et al., 2000; Deschamps and Trampert, 2003). Despite these advances, the origin and evolution of LLSVPs are not constrained.

Many geodynamic studies have investigated dynamical hypotheses that may give rise to seismically observed LLSVPs (e.g., Tackley, 1998; Thompson and Tackley, 1998; Davaille, 1999; Kellogg et al., 1999; Hansen and Yuen, 2000; Tackley, 2000; Jellinek and Manga, 2002;

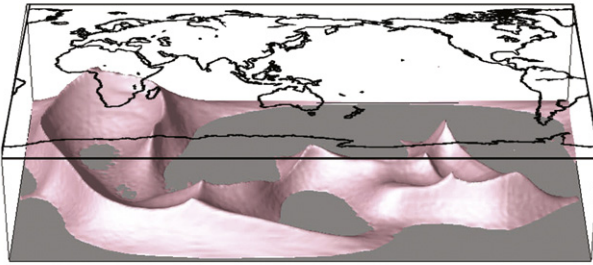
Davaille et al., 2002, 2003; Jellinek and Manga, 2004; Schubert et al., 2004; McNamara and Zhong, 2004, 2005; Tan and Gurnis, 2005; Ritsema et al., 2007; Tan and Gurnis, 2007; Deschamps and Tackley, 2008; Garnero and McNamara, 2008; Bull et al., 2009). Here, we focus on two competing dynamic hypotheses: (a) compositionally distinct piles of dense material at the base of the mantle, hereafter called “thermochemical piles” (Fig. 1B) (e.g., Tackley, 1998; Kellogg et al., 1999; Tackley, 2000; Hansen and Yuen, 2000; Jellinek and Manga, 2002, 2004; McNamara and Zhong, 2004, 2005; Tan and Gurnis, 2005, 2007; Nakagawa and Tackley, 2006; Deschamps and Tackley, 2008) and (b) geographically concentrated clusters of mantle plumes, hereafter denoted as “plume clusters” (Fig. 1C) (e.g., Schubert et al., 2004; Ritsema et al., 2007; Bull et al., 2009). In both hypotheses, subducting slabs descend to the base of the mantle, eventually guiding material away from downwelling regions, toward upwelling regions in the lower mantle beneath Africa and the central Pacific. In the thermochemical pile hypothesis, plumes rise from the topographical peaks of the piles of intrinsically dense material, whereas in the plume cluster hypothesis, plumes rise from the lowermost thermal boundary layer above the core–mantle boundary (CMB) in these upwelling regions. These 2 models represent end-member cases of how compositional heterogeneity may influence mantle dynamics. In the thermochemical piles model, compositional heterogeneity is dense enough to form long-lived, stable reservoirs. The plume cluster model differs from the thermochemical pile model in that compositional heterogeneity does not play a dynamic role, producing a style of convection that is dominated by thermal buoyancy forces. The result is an effectively isochemical system of

* Corresponding author. Tel./fax: +1 4809658102.
E-mail address: Teresa.Lassak@asu.edu (T.M. Lassak).

A) Shear-wave tomography



B) Thermochemical Piles



C) Plume Clusters

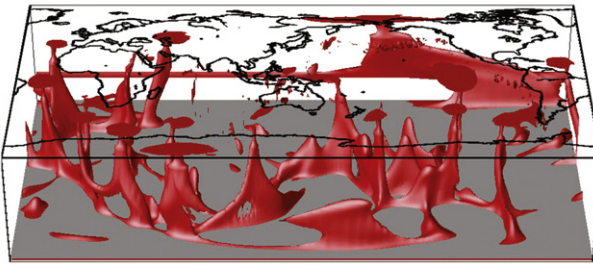


Fig. 1. (A) Shear-wave velocity heterogeneities from S20RTS tomography model (Ritsema et al. 1999, 2004) showing distinct, large, low shear-velocity anomalies in red. Two proposed models describing large, low shear-wave velocity anomalies: (B) thermochemical piles (reference case TC1 showing a compositional isosurface at $C = 0.5$); (C) plume clusters (reference case PC1 showing a temperature isosurface at $T = 0.69$).

convection. This is expected to occur if either the intrinsic density of compositional heterogeneity is similar to that of background mantle and/or if the thickness of compositional heterogeneity is much thinner than the lower thermal boundary layer, such that plumes form along the CMB in a manner similar to isochemical convection.

While thermochemical piles and plume clusters may both provide a feasible mechanism for explaining observations, such as geochemistry of OIBs and MORBs [e.g., Davaille, 1999; Kellogg et al., 1999; Tackley, 2000; Davaille et al., 2002; Jellinek and Manga, 2002; Davaille et al., 2003; Jellinek and Manga, 2004; Deschamps and Tackley, 2008], and the presence of LLSVPs in seismic tomography [e.g., Bull et al., 2009], they differ strongly in their distribution of deep mantle density perturbations, leading to significantly different mechanisms of mass and heat transport. Plume cluster models advect heat and compositional heterogeneity from the CMB to the top of the mantle, mixing both with the surrounding mantle. The result is a temperature structure that is relatively homogeneous and a compositional structure that is well-stirred. Thermochemical piles, on the other hand, lead to a very different thermal and compositional mantle structure. Heat transport out of the piles is limited by conduction and compositional transport is limited to the small amount of viscous entrainment that occurs via mantle plumes rising from the pile surface.

The topography at the CMB has been shown to depend critically upon dynamical processes within the mantle, namely the style of mantle

convection (e.g., Hide and Horai, 1968; Hager and Richards, 1989; Forte and Peltier, 1991; Lassak et al., 2007). We thus expect the nature of CMB topography to reflect the thermal, chemical and dynamical structure of the mantle. Geodynamic and geodetic studies have determined that topographic relief along the CMB should generally be depressed beneath regions of subduction and elevated beneath upwelling regions (e.g., Hide and Horai, 1968; Hide, 1969; Hager and Richards, 1989; Forte et al., 1995; Steinberger and Holme, 2008; Yoshida, 2008). Studies involving the variations in Earth's rotation, which relate to the geometry of the CMB, provide guides for general CMB shape and may potentially aid in constraining the topography along the CMB at longer wavelength (e.g., Gwinn et al., 1986; Buffett et al., 2000; Mathews et al., 2002).

There have been numerous efforts to seismically determine CMB topography (e.g., Creager and Jordan, 1986; Morelli and Dziewonski, 1987; Gudmundsson et al., 1990; Li et al., 1991; Revenaugh and Jordan, 1991; Hide et al., 1993; Poupinet et al., 1993; Rodgers and Wahr, 1993; Murphy et al., 1997; Obayashi and Fukao, 1997; Sylvander et al., 1997; Ishii and Tromp, 1999; Boschi and Dziewonski, 2000; Castle and van der Hilst, 2000; Garcia and Souriau, 2000; Koper et al., 2003; Sze and van der Hilst, 2003). Resulting seismic models of CMB topography indicate long-wavelength patterns in CMB topography with amplitudes up to ± 6 km (e.g., Morelli and Dziewonski, 1987; Obayashi and Fukao, 1997; Boschi and Dziewonski, 2000) while more recent work has suggested smaller amplitudes of ± 1.5 km (Sze and van der Hilst, 2003).

In our previous work (Lassak et al., 2007), we investigated CMB topography resulting from plume cluster and thermochemical pile mantle models in two-dimensions (2D). We found that, despite the intrinsic density increase of a thermochemical pile, its effective density is similar to that of surrounding mantle due to a counteracting density decrease caused by thermal expansion. This leads to an overall reduction in topographic amplitude along the CMB, when compared to plume cluster models. Furthermore, CMB topographic relief beneath thermochemical piles was relatively flat and slightly positive compared to CMB topography beneath downwellings. In plume cluster models, there was a direct correlation between upwarping (positive) relief on the CMB and upwellings while downwarping (negative) relief occurred beneath downwelling regions. An important finding in that study is that the temperature-dependence of viscosity significantly affects CMB topographic relief beneath downwellings and piles, and therefore, cannot be excluded in this type of study. Lassak et al. (2007) provides important insight into the relationship between different dynamical mantle hypotheses and CMB topography; however, that study was limited to 2D and did not consider the effects of self-gravitation. As a result, we are motivated to investigate the relationship between mantle convection and CMB topography in three-dimensional (3D) spherical geometry, while including the effects of self-gravitation.

In this study, we investigate the CMB topography associated with thermochemical pile and plume cluster models. The goal is to document the effects of mantle convection on CMB topography. In the sections that follow, we show that our two different model types produce unique CMB topography signatures; thus as seismic studies better resolve the global topography of Earth's CMB, there is potential to constrain the chemical and dynamic nature of Earth's lower mantle.

2. Method

2.1. Governing equations

We solve the conservation equations of mass, momentum, energy and composition using the Boussinesq approximation. All "reference" variables (Table 1) are dimensional. Unless otherwise noted, all other variables are non-dimensional. The non-dimensional equation for conservation of mass is:

$$\nabla \cdot \vec{u} = 0, \quad (1)$$

where \vec{u} is the velocity field. The non-dimensional conservation of heat equation is:

$$\frac{\partial T}{\partial t} + \vec{u} \cdot \nabla T = \nabla^2 T + H, \quad (2)$$

where T is the temperature, t is time, and H is the internal heat generation.

The non-dimensional conservation of momentum equation is:

$$-\nabla P + \nabla \cdot [\eta(\nabla \vec{u} + \nabla^T \vec{u})] + \left[\xi Ra(T-BC) - \frac{R^3}{\eta_0 \kappa_0} \rho_0 \delta g \right] \mathbf{e}_r = 0, \quad (3)$$

where P is the dynamic pressure, η is the mantle viscosity, Ra is the Rayleigh number, B is the buoyancy number, η_0 is the reference viscosity, κ_0 is the reference thermal diffusivity, ρ_0 is the reference density, δg is the dimensional perturbation to radial gravitational acceleration and leads to self-gravitation, $\xi = R^3/h^3$, R is dimensional Earth radius, h is dimensional mantle thickness, and \mathbf{e}_r is the radial unit vector. Length is non-dimensionalized by Earth radius.

The perturbation to the radial gravitational acceleration, δg , is:

$$\delta g = (-\nabla \varphi)_r, \quad (4)$$

where φ is the dimensional perturbation to gravitational potential determined by Poisson's equation:

$$\nabla^2 \varphi = -4\pi G \delta \rho_{total}, \quad (5)$$

where G is the gravitational constant and $\delta \rho_{total}$ represents the dimensional density perturbations from reference state that corresponds to both internal density distributions and topography at the surface and CMB.

We introduce the “reduced” dynamic pressure P_R as follows:

$$P_R = P - \frac{R^2}{\eta_0 \kappa_0} \rho_0 \varphi, \quad (6)$$

and the conservation of momentum finally becomes:

$$-\nabla P_R + \nabla \cdot \eta(\nabla \vec{u} + \nabla^T \vec{u}) + \xi Ra(T-BC)\mathbf{e}_r = 0. \quad (7)$$

We define the thermal Rayleigh number (Ra): and the buoyancy number (B):

$$Ra = \frac{\rho_0 g \alpha_0 \Delta T h^3}{\eta_0 \kappa_0}; \quad B = \frac{\Delta \rho}{\rho_0 \alpha \Delta T}, \quad (8)$$

where ΔT is the dimensional temperature drop across the mantle, α_0 is the reference thermal expansivity, and $\Delta \rho$ is the dimensional intrinsic density contrast between compositions. B is a non-dimen-

Table 1

Physical reference values used in the calculations. Note that reference viscosity is modified for calculations TC4, TC5, PC4, and PC5.

Symbol	Description	Value	Dimensional units
ρ_0	Reference density	3300	kg m ⁻³
g_0	Acceleration of gravity	10	m s ⁻²
κ_0	Reference thermal diffusivity	10 ⁻⁶	m ² s ⁻¹
ΔT	Temperature drop across the mantle	3000	K
α	Reference thermal expansivity	10 ⁻⁵	K ⁻¹
R	Earth radius	6.371 × 10 ⁶	m
R_{CMB}	CMB radius	3.480 × 10 ⁶	m
d	Mantle thickness	2.891 × 10 ⁶	m
η_0	Reference viscosity	1.70 × 10 ²⁰	Pa s
$\Delta \rho_{cmb}$	Density contrast across the CMB	4430	kg m ⁻³
$\Delta \rho_{surface}$	Density contrast across the surface	3300	kg m ⁻³

sional quantity that is a measure of the intrinsic density contrast in the thermochemical models. The non-dimensional equation for chemical advection is:

$$\frac{\partial C}{\partial t} + (\nabla \cdot \vec{u})C = 0, \quad (9)$$

where C is the coefficient representing compositional heterogeneity, that initially equals 1 and 0 for pile material and background mantle, respectively. We use the following dimensional equation of state:

$$\delta \rho(T, C) = -\rho_0 \alpha_0 (T_d - T_o) + \Delta \rho C, \quad (10)$$

where T_o is the reference temperature, T_d is the dimensional temperature, and $\delta \rho(T_d = T_o, C = 0) = 0$. For isochemical calculations, Eq. (10) simplifies to:

$$\delta \rho = -\rho_0 \alpha_0 (T_d - T_o). \quad (11)$$

We use the following formulation for viscosity:

$$\eta(T, z) = \eta_r(z) \exp[A(0.5 - T)], \quad (12)$$

where η_r represents the viscosity depth-dependence, z represents dimensional depth in km, A represents the activation coefficient that controls the temperature-dependence of viscosity, and T is the temperature. For all cases, $\eta_r = 1$ for the upper mantle ($z < 660$ km) and for the lower mantle. Following this definition, we model a weak upper mantle with a 30× viscosity jump at the 660 km discontinuity and a 10× linear increase with depth from the top of the lower mantle to the CMB. We define, and use hereafter, the term “viscosity contrast” $\Delta \eta = \exp(A)$ as a measure of temperature-dependence which represents the ratio of maximum to minimum possible viscosity (e.g. a contrast between the hottest and the coldest).

The non-dimensional radial stress (σ_{rr}) acting on a surface is:

$$\sigma_{rr} = 2\eta \dot{\epsilon}_{rr} - P, \quad (13)$$

where $\dot{\epsilon}_{rr}$ is the strain rate. Since we define our dynamic pressure as a “reduced” dynamic pressure, and the stress at a boundary is a function of dynamic pressure, we rewrite Eq. (13) using Eq. (6):

$$\begin{aligned} \sigma_{rr} &= 2\eta \dot{\epsilon}_{rr} - \left(P_R + \frac{R^2}{\eta_0 \kappa_0} \rho_0 \varphi \right) \Rightarrow \sigma_{rr} = (2\eta \dot{\epsilon}_{rr} - P_R) - \frac{R^2}{\eta_0 \kappa_0} \rho_0 \varphi \Rightarrow \\ \sigma_{rr} &= \tilde{\sigma}_{rr} - \frac{R^2}{\eta_0 \kappa_0} \rho_0 \varphi, \end{aligned} \quad (14)$$

where $\tilde{\sigma}_{rr} = 2\eta \dot{\epsilon}_{rr} - P_R$. Following the method of Zhang and Christensen (1993) and Zhong et al. (2008), the equations for dimensional surface topography (s) and CMB topography (b) become:

$$s = -\frac{\left(\frac{\kappa_0 \eta_0}{R^2}\right) \tilde{\sigma}_{surface} - \Delta \rho_{surface} \varphi_{surface}}{\Delta \rho_{surface} g_0}; \quad b = \frac{\left(\frac{\kappa_0 \eta_0}{R^2}\right) \tilde{\sigma}_{cmb} + \Delta \rho_{cmb} \varphi_{cmb}}{\Delta \rho_{cmb} g_0}, \quad (15)$$

where $\Delta \rho_{surface}$ and $\Delta \rho_{cmb}$ are the density contrasts across the top and bottom boundaries, respectively, and $\tilde{\sigma}_{surface}$ and $\tilde{\sigma}_{cmb}$ are the stresses on the top and bottom boundaries, respectively. Ricard et al. (1984) also considered CMB dynamic topography with self-gravitation.

2.2. Computational method

We use the thermochemical extension of CitcomS, a three-dimensional (3D) spherical finite-element thermochemical convection

code (Zhong et al., 2000; McNamara and Zhong, 2004), to solve the conservation equations for a series of whole mantle convection calculations, which correspond to different dynamical hypotheses. We track compositional evolution via advection tracers by employing the ratio tracer method as reviewed and tested in Tackley and King (2003) and McNamara and Zhong (2004). The calculations employ 64 elements radially and 49,152 elements laterally (3.15 million total elements) with an average of 24 tracers per element. Elements are refined in the radial direction in the upper mantle and lowermost 700 km of the lower mantle. Each calculation was divided between 48 processor domains and solved in parallel. We performed resolution tests to confirm that this resolution is more than adequate for all cases in this study.

Using the temperature and compositional fields derived from our calculations, we calculate internal density distributions and their resulting contributions to the gravitational potential, and the topography along the surface and bottom model boundaries. We decompose the stresses along the surface and bottom boundaries into spherical harmonics, and then use these along with Poisson's Eq. (5) to calculate the perturbations to the gravitational potential, and the topography along the surface and bottom model boundaries. Boundary conditions for the gravitational potential are 0 at infinity and continuity at the density interfaces (e.g., Zhong et al., 2003). Further details for the full-method and post-processing steps required can be found in Zhong et al. (2008). Our calculation for topography was tested against the benchmarks included in Zhong et al. (2008).

CMB topography is calculated from a Stokes flow calculation employing free-slip velocity boundary conditions. Temperature boundary conditions are 0 and 1 at the top and bottom boundaries, respectively. The initial condition for temperature and composition are derived from a time-dependent calculation that employs surface plate motions for the past 119 million years (e.g., Ricard et al., 1993; Lithgow-Bertelloni and Richards, 1998) in order to provide plausible locations of historical subduction (as used in McNamara and Zhong, 2005). This allows for the development of slabs in the mantle, roughly consistent with geologic history. These slabs drive the mantle flow, leading to upwelling centers beneath Africa and the Pacific (e.g., McNamara and Zhong, 2005). The 119 million year time-dependent calculation is initiated using the temperature profile derived from a 2D axi-symmetric convection calculation that has reached a steady state. All calculations are heated from below as well as internally with a non-dimensional heat production of 10, which leads roughly to heating that is half internal and half bottom.

3. Results

We present a series of plume cluster (denoted by the abbreviation PC) and thermochemical pile (denoted by the abbreviation TC) cases. All calculations are listed in Table 2. Our reference cases for thermochemical piles and plume clusters are illustrated in Figs. 1 and 2. Reference case parameters are: $Ra = 1.4e8$ and $\Delta\eta = 1e4$. We investigated the effect of self-gravitation, variations in temperature-dependence of viscosity, changes in Rayleigh number, variations in initial pile thickness, and buoyancy number for pile models (Fig. 3A–H) and plume cluster models (Fig. 3I–L). Here we will highlight the important aspects of each model and the resulting CMB topographic relief.

3.1. Thermochemical piles

Plots of CMB topography for our reference pile case, TC1, are shown in Fig. 2A and B. In our two-dimensional (2D) work (Lassak et al., 2007), we calculated CMB topography without incorporating the effect of self-gravitation. Here, we show the calculated CMB topography for our three-dimensional (3D) piles model, TC1, without (Fig. 2A) and with self-gravitation (Fig. 2B–C). CMB topographic relief beneath thermochemical pile regions is generally positive (here, “positive relief” on the CMB refers to the CMB being elevated towards the surface of the Earth, away from the core). The overall pattern of CMB topography in the pile model is

Table 2

Cases presented. Thermochemical cases are represented by the prefix TC; and plume cluster cases are represented by the prefix PC. Ra is the Rayleigh number, d is the initial layer thickness, $\Delta\eta$ is the temperature-dependence of viscosity, and B is the buoyancy number.

Case	Fig.	$\Delta\eta$	Ra	d	B number
TC1	1B, 2A–E	10^4	$1.40E+08$	255	0.6
TC2	3A	10^3	$1.40E+08$	255	0.6
TC3	3B	10^5	$1.40E+08$	255	0.6
TC4	3C	10^4	$1.40E+07$	255	0.6
TC5	3D	10^4	$1.40E+09$	255	0.6
TC6	3E	10^4	$1.40E+08$	150	0.6
TC7	3F	10^4	$1.40E+08$	396	0.6
TC8	3G	10^4	$1.40E+08$	255	0.5
TC9	3H	10^4	$1.40E+08$	255	0.7
TC10	4	10^4	$1.40E+08$	255	0.6
PC1	1C, 2F–J	10^4	$1.40E+08$	–	–
PC2	3I	10^3	$1.40E+08$	–	–
PC3	3J	10^5	$1.40E+08$	–	–
PC4	3K	10^4	$1.40E+07$	–	–
PC5	3L	10^4	$1.40E+09$	–	–

broad regions of positive relief beneath the interiors of piles. Narrow ridges with high, positive relief mark the perimeter of pile regions; these are a prominent feature observed in all thermochemical pile cases that we tested. Negative relief (the CMB is depressed away from the surface of the Earth, toward the core) occurs beneath regions of long-lived subduction. These topographic relief features are present with and without self-gravitation (Fig. 2B and A, respectively), and only exhibit minor differences at long wavelengths (which is visible in the power spectrum representation in Fig. 2D) (Zhong et al., 2008). The areal distribution of the CMB topographic relief is illustrated in Fig. 2E. In thermochemical pile models, there is a skewed distribution of positive and negative relief, with more area possessing positive CMB relief.

3.2. Plume clusters

CMB topography for our reference plume cluster case, PC1, without and with self-gravitation is shown in Fig. 2F and G, respectively. CMB topographic relief beneath upwelling plume cluster regions is exclusively positive, while negative topography occurs solely beneath regions of subduction. Both of these topographic relief patterns are observable with and without self-gravitation (Fig. 2G–H and F, respectively). Differences between CMB topography results in Fig. 2F and G are minor and are primarily evident only at long wavelengths (Fig. 2I), while differences in topographic relief appear to be negligible at smaller wavelengths (degrees greater than 6 or 8). In the plume cluster cases, the areal distribution of topography (Fig. 2J) is such that there is an apparent even areal distribution of positive and negative relief.

3.3. Temperature-dependence of viscosity

We vary the activation coefficient in both models to examine whether a change in the temperature-dependence of viscosity will affect the characteristic style of CMB topography. Reducing the temperature-dependence of viscosity by an order of magnitude ($\Delta\eta = 10^3$) leads to CMB topography shown in Fig. 3A (piles, Case TC2) and Fig. 3I (plume clusters, Case PC2). Increasing the temperature-dependence of viscosity by an order of magnitude ($\Delta\eta = 10^5$) leads to CMB topography shown in Fig. 3B (piles, Case TC3) and Fig. 3J (plume clusters, Case PC3). These results show that the characteristic pattern of CMB topography for each model is relatively insensitive to changes in the temperature-dependence of viscosity, consistent with our previous 2D work (Lassak et al., 2007).

3.4. Reference viscosity

We vary the Rayleigh number in both models to examine how sensitive our results are to the reference viscosity. Increasing the reference

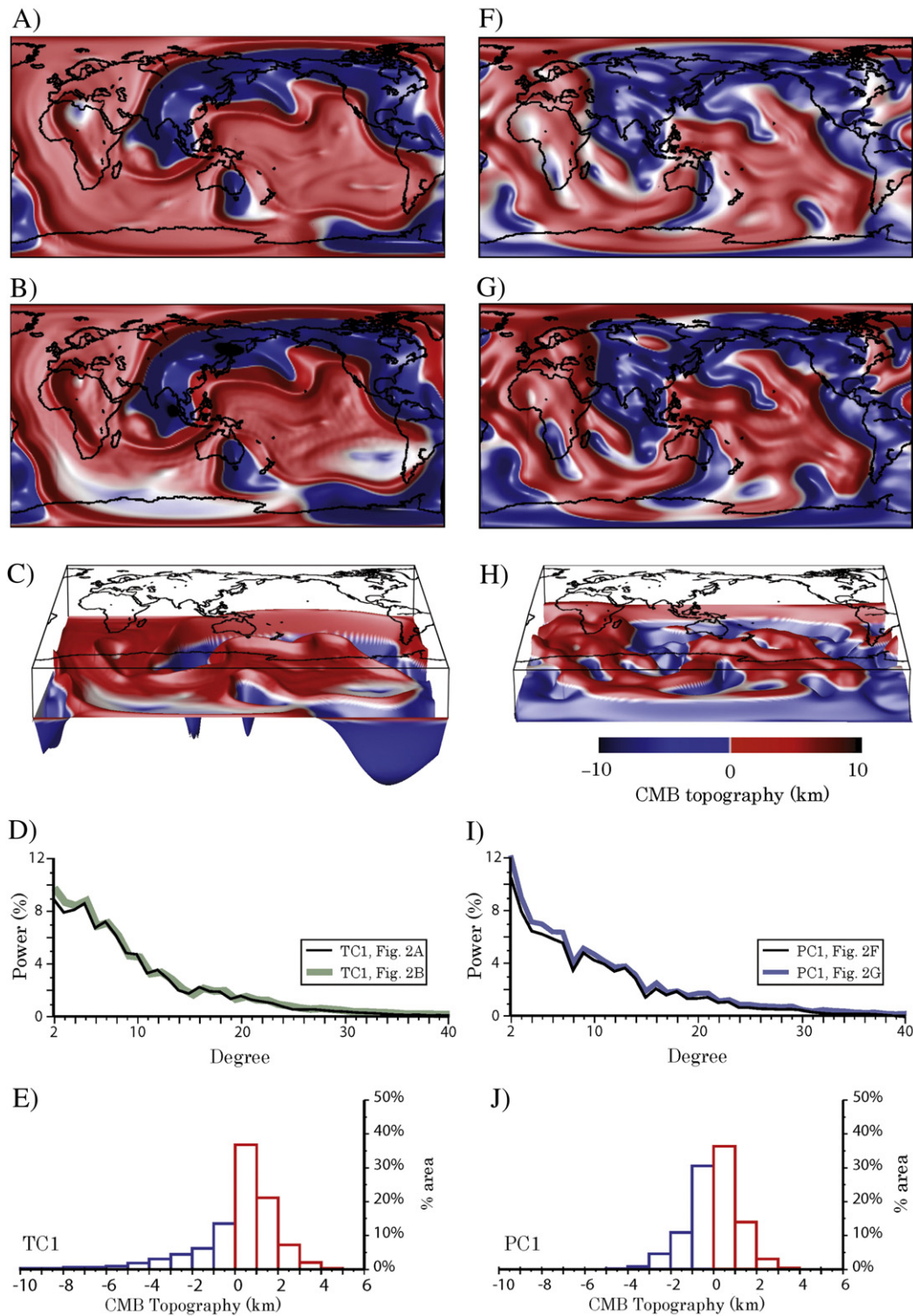


Fig. 2. CMB topography results in map view for thermochemical pile case TC1 (A) without self-gravitation and (B) with self-gravitation. (C) Perspective view of CMB topography with self-gravitation. (D) A power spectra plot that relates the CMB topography data distribution at each harmonic degree for case TC1 with and without self-gravitation. (E) A histogram shows the distribution of the positive and negative topographic relief areas for case TC1. CMB topography results in map view for plume cluster case PC1 (F) without self-gravitation and (G) with self-gravitation. (H) Perspective view of CMB topography with self-gravitation. (I) A power spectra plot that relates the CMB topography data distribution at each harmonic degree for case TC1 with and without self-gravitation. (J) A histogram shows the areal distribution of positive and negative topographic relief for case PC1. All plots are Cartesian projection of spherical geometry.

viscosity an order of magnitude (i.e., reducing the Rayleigh number an order of magnitude) leads to increased CMB topography amplitude in both models (piles, Case TC4, Fig. 3C; plume clusters, Case PC4, Fig. 3K). Similarly, decreasing the reference viscosity an order of magnitude (i.e., increasing the Rayleigh number an order of magnitude) leads to

decreased CMB topography amplitude in both models (piles, Case TC5, Fig. 3D; plume clusters, Case PC5, Fig. 3L). We find that changing the reference viscosity has a direct influence on CMB topography amplitude; however, the characteristic patterns of CMB topography for each model remain unchanged. It follows that a layer of reduced intrinsic viscosity in

the lowermost mantle would be expected to reduce CMB topography amplitude (Yoshida, 2008).

3.5. Volume of thermochemical piles

Our reference thermochemical pile case (TC1) employs a volume of intrinsically more dense material that is equivalent to a 255 km thick layer along the CMB. Here, we investigate the sensitivity of CMB topography to the volume of pile material. We find that decreasing the volume to an equivalent layer thickness of 150 km reduces the small amount of area within pile interiors that exhibits negative topography (Case TC6, Fig. 3E). Note that the slivers of slightly negative topography within pile interiors in the reference case (Case TC1, Fig. 2B) become smaller in Case TC6. Increasing the initial layer thickness to 396 km leads to a greater variability of topographic relief within pile interiors, with an increased area exhibiting negative topography (Case TC7, Fig. 3F). We interpret these results as the consequence of increased convective vigor within thermochemical piles as their volume increases. Convective vigor is sensitive to geometry (i.e., the h^3 dependence of Rayleigh number). Increasing the local Rayleigh number within a pile by increasing its volume, keeping reference viscosity fixed, will lead to higher convective stresses which lead to higher CMB topography amplitudes. For large piles, such as those in Case TC7, internal convection patterns will result in larger CMB topography variability within pile interiors.

3.6. Buoyancy number

The reference thermochemical pile case (TC1) utilizes a buoyancy number of 0.6. To investigate sensitivity of CMB topography to buoyancy number (i.e., intrinsic density of pile material), we investigate buoyancy numbers of 0.5 (Case TC8, Fig. 3G) and 0.7 (Case TC9, Fig. 3H). We find that smaller buoyancy numbers lead to unstable piles that quickly overturn, and larger buoyancy numbers cause pile material to flatten out into a layer along the CMB. In fact, for a given value of Rayleigh number, there is only a narrow range of buoyancy numbers that lead to stable, long-lived thermochemical piles. The lower buoyancy number case leads to increased amplitude of CMB topography within pile interiors (Fig. 3G). Like the reference case, the perimeter of the piles is marked by a ridge of positive CMB topography. Case TC8 also exhibits a ridge of positive topography within the interior of the Pacific pile, not unlike one of the linear segments of positive topography observed beneath plumes in the plume cluster model. A pile undergoing the transition from being stable to unstable would likely have a CMB topography that has a characteristic pattern that is intermediate between pile and plume cluster cases.

4. Discussion

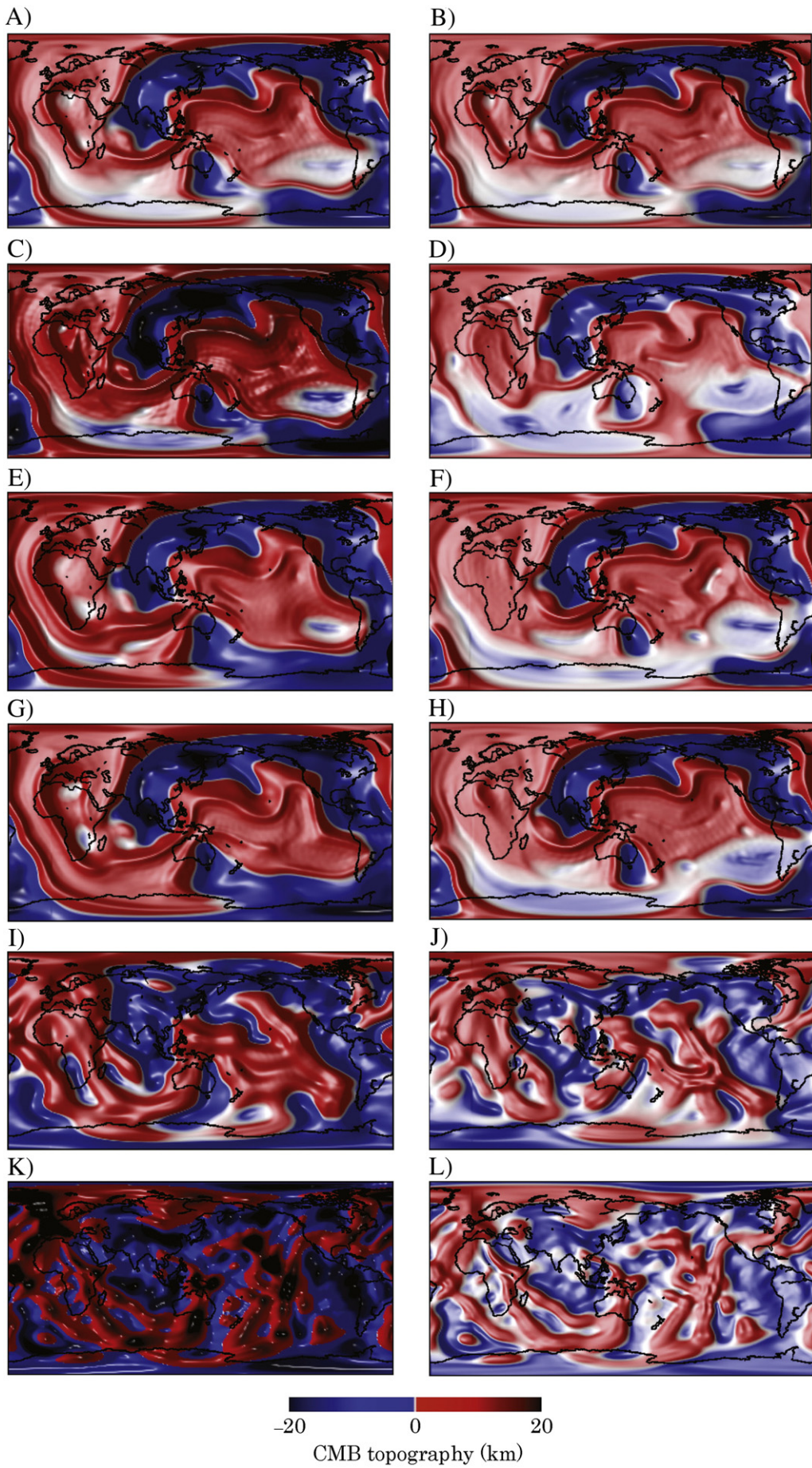
A primary motivation for this study was to assess if seismically determined CMB topography maps are capable of discriminating between proposed end-member geodynamical mantle models. We focused on two models: thermochemical piles and plume clusters. In both models, there is negative topographic relief beneath regions of ancient subduction. In the thermochemical pile model (Fig. 2B), the most prominent characteristic of CMB topography is broad regions of positive relief beneath piles, flanked by pronounced, higher, positive relief ridges. These perimeter ridge features are unique to the thermochemical pile models. Pile interiors are significantly hotter than background mantle, leading to dramatic reduction in viscosity. This results in lower radial stresses, hence low amplitude CMB topography. Therefore topographic relief is relatively flattened within pile interiors. Along pile perimeters, pile material is viscously coupled to the adjacent background mantle. The high positive topography along the pile perimeter is likely due to the higher viscosity of the cooler background mantle that flows upward along with pile material. The higher viscosity leads to greater radial stress, hence a larger amplitude of CMB topography, relative to that formed within the interior of piles. In the plume cluster model (Fig. 2G),

the most prominent characteristic of CMB topography is the high-relief ridges at the base of upwelling plumes. Ridges in the plume cluster model are prominent and distinctive features that are present beneath the plumes. The dense collection and abundance of high-relief ridges are unique to plume cluster models.

The buoyancy structure for these calculations was derived from a time-dependent mantle convection calculation that used kinematic velocity boundary conditions corresponding to plate motions for the past 119 million years. This allowed us to model structures that would be consistent with the global convection patterns expected for an Earth-like planet with plate tectonics. To ensure that our conclusions are not dependent upon that particular initial condition, we performed a much longer (1.4 billion years) time-dependent thermochemical convection calculation with free-slip velocity boundary conditions, using the same parameters as case TC1 except that the initial condition is a 1D temperature profile taken from a 2D axisymmetric calculation that has reached thermal equilibrium. This calculation, Case TC10, is shown in Fig. 4A–C. CMB topography (Fig. 4C) is characteristically similar to that observed in the reference thermochemical pile case, TC1. Negative CMB topography occurs beneath downwellings. CMB topography beneath piles is positive. CMB topography is relatively flat within pile interiors with peaks along pile perimeters. Because Case TC10 does not employ plate motions to produce an Earth-similar distribution of subduction, the geographic distribution of features should not be compared to neither Earth nor previous cases.

In order to explore the differences in CMB topography patterns between our thermochemical pile and plume cluster models at long-wavelength scale, we expand the CMB topography in cases TC1 and PC1 only out to degree 4 (Fig. 5A and B), which is the maximum degree presented in many CMB topography seismic studies (e.g., Creager and Jordan, 1986; Morelli and Dziewonski, 1987; Gudmundsson et al., 1990; Obayashi and Fukao, 1997; Boschi and Dziewonski, 2000; Sze and van der Hilst, 2003). The characteristic differences in topographic relief between the thermochemical pile and plume cluster models are not apparent at these longer wavelengths. Namely, the ridges along the perimeter of the broad, positive relief beneath the thermochemical piles (Fig. 2B) are not observed when limited to long wavelengths (degree 4, Fig. 5A). Similarly, the positive relief ridges beneath upwellings in the plume cluster model (Fig. 2E) are not detectable at lower spherical harmonic degrees (degree 4, Fig. 5B). In fact, both models appear quite similar at this lower resolution. In order to distinguish between different geodynamic model predictions, shorter-wavelength CMB topographic relief information is necessary. By comparing topography maps of both models as we increase the harmonic degree, we find that topography characteristics unique to each model begin to significantly stand out above degree 15.

It is important to note the uncertainties associated with our thermochemical pile and plume cluster models. While we use a best estimate of material properties, some parameters are only loosely constrained (e.g., rheological formulation, the Rayleigh number, volume of pile material). By varying these, we find differences in CMB topography amplitude; however, the overall characteristic style of topography remains. Furthermore, the plate motions used to construct the buoyancy structure likely contain errors, particularly for older times, so it is important not to directly compare specifics in our results to a particular geographical location. Also, if thermochemical convection is occurring in Earth's mantle, it may be more complex than these simple models can reproduce, or it may take a different form, such as thermochemical superplumes (e.g., Davaille, 1999). Finally our models do not include the recently discovered post-perovskite phase transition which may exist in the cooler regions of the lowermost mantle (Shim et al., 2001; Murakami et al., 2004; Oganov and Ono, 2004; Tsuchiya et al., 2004; Hirose and Fujita, 2005). Post-perovskite is denser than perovskite, so its presence in downwelling regions at the CMB (e.g., Nakagawa and Tackley, 2008) could



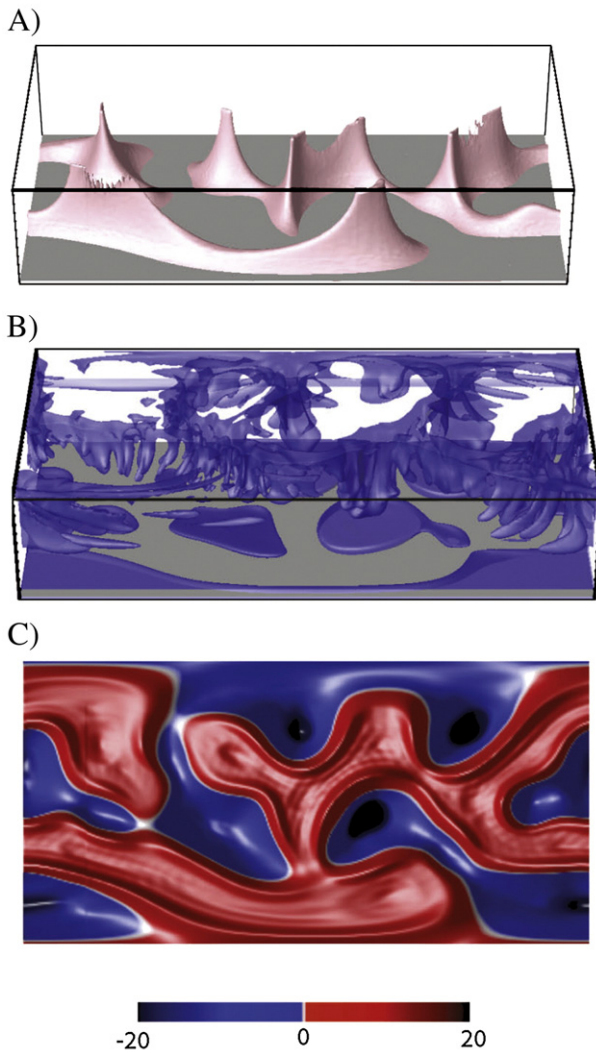


Fig. 4. (A) Thermochemical piles from case TC10 (compositional isocontour at $C = 0.5$). (B) Cold downwellings are shown at residual temperature isocontour -0.15 . (C) CMB topography results in map view for thermochemical pile case TC10. All plots are Cartesian projection of spherical geometry.

act to magnify the negative topography found in these regions of our study, but it is not expected to have an influence in pile or plume cluster regions.

5. Conclusions

We show that the thermochemical pile and plume cluster models produce a unique style of topographic relief along the CMB; therefore, seismically determined CMB topography may eventually become useful in discriminating between the different proposed mantle models. We conclude:

1) CMB topography in thermochemical pile models: The overall pattern of CMB topography for the thermochemical pile model is broad

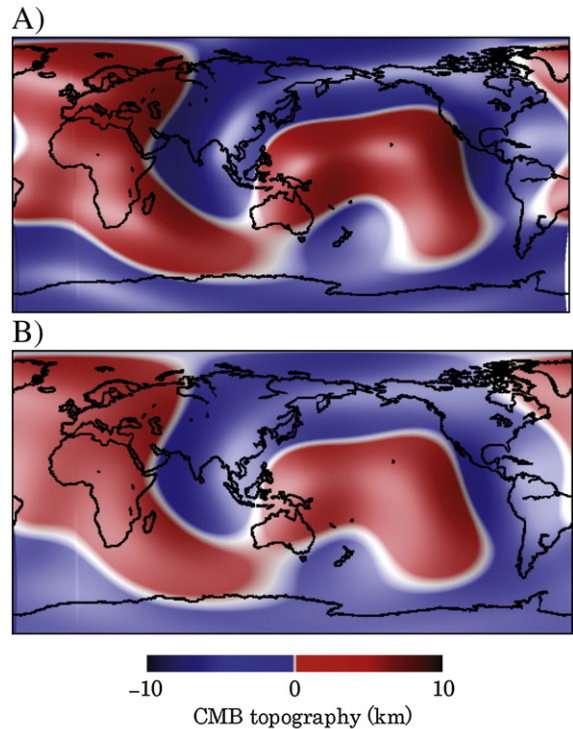


Fig. 5. Long-wavelength (degree = 4) CMB topography results for (A) thermochemical pile case TC1, and (B) plume cluster case PC1.

regions of positive relief. Narrow ridges with high, positive relief mark the perimeter of pile regions; this is a prominent feature. Negative topography occurs predominantly beneath regions of ancient subduction.

- 2) CMB topography in plume cluster models: The pattern of CMB topography, in plume cluster models, is positive topographic relief along the base of plumes and any area of upwelling. Negative topography occurs solely beneath regions of ancient subduction.
- 3) Effects of self-gravitation on CMB topography: Including self-gravitation does not significantly affect the resulting CMB topography. Overall, the differences between CMB topography results with and without self-gravitation are minor and any differences would reside in the lower harmonic degrees (<4). Major characteristic topography patterns for both the thermochemical pile models and plume cluster models are present when calculating topography without self-gravitation as when calculating topography with self-gravitation.
- 4) Importance of small-scale structure: In order to identify a specific mantle model for Earth's mantle using CMB topography, it is necessary to resolve smaller-scale ($>$ degree 15) topography structure. Current seismic models of CMB topography are limited to lower harmonic degrees (<4). Future seismic studies that image smaller-scale CMB topography structure will be extremely useful in better resolving the pattern of topography on Earth's CMB.

Fig. 3. CMB topography results for thermochemical pile cases, in map view. All cases are listed in Table 1: (A) In case TC2, temperature-dependence of viscosity is decreased ($\Delta\eta = 10^3$); (B) In case TC3, temperature-dependence of viscosity is increased ($\Delta\eta = 10^5$); (C) In case TC4, Rayleigh number is decreased ($Ra = 1.4e7$); (D) In case TC5, Rayleigh number is increased ($Ra = 1.4e9$); (E) In case TC6, initial layer thickness is decreased ($d = 150$ km); (F) In case TC7, initial layer thickness is increased ($d = 396$ km). (G) In case TC8, the buoyancy number is decreased ($B = 0.5$); (H) In case TC9, the buoyancy number is increased ($B = 0.7$). CMB topography results for plume cluster cases, in map view: (I) In case PC2, temperature-dependence of viscosity is decreased ($\Delta\eta = 10^3$); (J) In case PC3, temperature-dependence of viscosity is increased ($\Delta\eta = 10^5$); (K) In case PC4, Rayleigh number is decreased ($Ra = 1.4e7$); (L) In case PC5, Rayleigh number is increased ($Ra = 1.4e9$). All plots are Cartesian projection of spherical geometry.

Acknowledgements

National Science Foundation grants EAR-0456356, EAR-0510383, EAR-0711366, and EAR-0838565 provided funds for this research. We thank Frank Timmes and the ASU HPC for allowing us to use their resources for our calculations. We also extend our gratitude to Thorsten Becker, Amanda Clark, Matt Fouch, Jim Tyburczy, and Abigail Bull for fruitful discussions. Reviews and comments from Yanick Ricard, Masaki Yoshida, and an anonymous reviewer enhanced the manuscript greatly.

References

- Boschi, L., Dziewonski, A.M., 2000. Whole Earth tomography from delay times of P, PcP, PKP phases: lateral heterogeneities in the outer core, or radial anisotropy in the mantle? *J. Geophys. Res.* 105, 13675–13696.
- Buffett, B.A., Gamero, E.J., Jeanloz, R., 2000. Sediments at the top of Earth's core. *Science* 290, 1338–1342.
- Bull, A.L., McNamara, A.K., Ritsema, J., 2009. Synthetic tomography of plume clusters and thermochemical piles. *Earth Planet. Sci. Lett.* 278, 152–162.
- Castle, J.C., van der Hilst, R.D., 2000. The core–mantle boundary under the Gulf of Alaska: no ULVZ for shear waves. *Earth Planet. Sci. Lett.* 176 (3–4), 311–321.
- Creager, K., Jordan, T., 1986. Aspherical structure of the core–mantle boundary from PKP travel times. *Geophys. Res. Lett.* 13, 1497–1500.
- Davaille, A., 1999. Simultaneous generation of hotspots and superswells by convection in a heterogeneous planetary mantle. *Nature* 402, 756–760.
- Davaille, A., Girard, F., Le Bars, M., 2002. How to anchor hotspots in a convecting mantle? *Earth Planet. Sci. Lett.* 203, 621–634.
- Davaille, A., Le Bars, M., Carbonne, C., 2003. Thermal convection in a heterogeneous mantle. *Geoscience* 335, 141–156.
- Deschamps, F., Tackley, P.J., 2008. Searching for models of thermo-chemical convection that explain probabilistic tomography I. Principles and influence of rheological parameters. *Phys. Earth Planet. Inter.* 171, 357–373.
- Deschamps, F., Trampert, J., 2003. Mantle tomography and its relation to temperature and composition. *Phys. Earth Planet. Inter.* 140, 277–291.
- Dziewonski, A.M., 1984. Mapping the lower mantle – determination of lateral heterogeneity in P-velocity up to degree and order-6. *J. Geophys. Res.* 89 (B7), 5929–5952.
- Ford, S.R., Garnero, E.J., McNamara, A.K., 2006. A strong lateral shear velocity gradient and anisotropy heterogeneity in the lowermost mantle beneath the southern Pacific. *J. Geophys. Res.* 111 (B3) Art. No. B03306.
- Forté, A.M., Mitrovica, J.X., Woodward, R.L., 1995. Seismic–geodynamic determination of the origin of excess ellipticity of the core–mantle boundary. *Geophys. Res. Lett.* 22 (9), 1013–1016.
- Forté, A.M., Peltier, W.R., 1991. Mantle convection and core–mantle boundary topography: explanations and implications. *Tectonophysics* 187, 91–116.
- García, R., Souriau, A., 2000. Amplitude of the core–mantle boundary topography estimated by stochastic analysis of core phases. *Phys. Earth Planet. Inter.* 117, 345–359.
- Garnero, E.J., McNamara, A.K., 2008. Structure and dynamics of Earth's lower mantle. *Science* 320. doi:10.1126/science.1148028, 626–628.
- Grand, S.P., van der Hilst, R.D., Widiyantoro, S., 1997. Global seismic tomography: a snapshot of convection in the Earth. *GSA Today* 7, 1–7.
- Gudmundsson, O., Davie, J.H., Clayton, R.W., 1990. Stochastic-analysis of global traveltime data – mantle heterogeneity and random errors in the ISC data. *Geophys. J. Int.* 102 (1), 25–43.
- Gwinn, C.R., Herring, T.A., Shapiro, I.L., 1986. Geodesy by radio interferometry—studies of the forced nutations of the Earth. *J. Geophys. Res.* 91 (B5), 4755–4765.
- Hager, B.H., Richards, M.A., 1989. Long-wavelength variations in Earth's geoid: physical models and dynamical implications. *Phil. Trans. R. Soc. Lond.* 328, 309–327.
- Hansen, U., Yuen, D., 2000. Extended-Boussinesq thermal-chemical convection with moving heat sources and variable viscosity. *Earth Planet. Sci. Lett.* 176, 401–411.
- Hide, R., 1969. Interaction between Earth's liquid core and solid mantle. *Nature* 222 (5198), 1055–1056.
- Hide, R., Horai, K., 1968. On the topography of the core–mantle interface. *Phys. Earth Planet. Inter.* 1, 305–308.
- Hide, R., Clayton, R.W., Hager, B.H., Spieth, M.A., Voorhies, C.V., 1993. Topographic core–mantle coupling and fluctuations in the Earth's rotation. *Jeffreys Volume Geophysical Monograph* 76, vol. 16. IUGG, pp. 107–120.
- Hirose, K., Fujita, Y., 2005. Clapeyron slope of the post-perovskite phase transition in CaFeO₃. *Geophys. Res. Lett.* 32, L13313. doi:10.1029/2005GL023219, 2005.
- Hofmann, A.W., 1997. Mantle geochemistry: the message from oceanic volcanism. *Nature* 385, 219–229 1997.
- Ishii, M., Tromp, J., 1999. Normal-mode and free-air gravity constraints on lateral variations in velocity and density of Earth's mantle. *Science* 285, 1231–1236.
- Jellinek, A.M., Manga, M., 2002. The influence of a chemical boundary layer on the fixity, spacing, and lifetime of mantle plumes. *Nature* 418, 760–763.
- Jellinek, A.M., Manga, M., 2004. Links between long-lived hot spots, mantle plumes, D^{''}, and plate tectonics. *Rev. Geophys.* 42 2003RG000144.
- Kellogg, L.H., Hager, B.H., van der Hilst, R.D., 1999. Compositional stratification in the deep mantle. *Science* 283, 1881–1884.
- Koper, K.D., Pyle, M.L., Franks, J.M., 2003. Constraints on Aspherical core structure from PKIKP–PCP differential travel-times. *J. Geophys. Res.* 108 (B3). doi:10.1029/2002JB001995.
- Lassak, T.M., McNamara, A.K., Zhong, S., 2007. Influence of thermochemical piles on topography at Earth's core–mantle boundary. *Earth Planet. Sci. Lett.* 261, 443–445.
- Li, X.D., Giardini, D., Woodhouse, J.H., 1991. Large-scale 3-dimensional even-degree structure of the Earth from splitting of long-period normal modes. *J. Geophys. Res.* 96 (B1), 551–577.
- Lithgow-Bertelloni, C., Richards, M.A., 1998. The dynamics of Cenozoic and Mesozoic plate motions. *Rev. Geophys.* 36, 27–78.
- Masters, G., Laske, G., Bolton, H., Dziewonski, A.M., 2000. The relative behavior of shear velocity, bulk sound speed, and compressional velocity in the mantle: implications for chemical and thermal structure. In: Karato, S., et al. (Ed.), *Earth's Deep Interior: Mineral Physics and Tomography from the Atomic to the Global Scale*. American Geophysical Union, Washington, DC, pp. 63–87.
- Mathews, P.M., Herring, T.A., Buffett, B.A., 2002. Modeling of nutation and precession: new nutation series for non-rigid Earth and insights into the Earth's interior. *J. Geophys. Res.* 107 (B4). doi:10.1029/2001JB000390.
- McNamara, A.K., Zhong, S., 2004. Thermochemical structures within a spherical mantle: superplumes or piles? *J. Geophys. Res.* 109. doi:10.1029/2003JB002847.
- McNamara, A.K., Zhong, S., 2005. Thermochemical piles under Africa and the Pacific. *Nature* 437. doi:10.1038/nature04066.
- Mégnin, C., Romanowicz, B., 2000. The shear-wave velocity structure of the mantle from the inversion of body, surface and higher modes waveforms. *Geophys. J. Int.* 143, 709–728.
- Morelli, A., Dziewonski, A.M., 1987. Topography of the core–mantle boundary and lateral homogeneity of the liquid core. *Nature* 325, 678–683.
- Murakami, M., Hirose, K., Kawamura, K., Sata, N., Ohishi, Y., 2004. Post-perovskite phase transition in MgSiO₃. *Science* 304. doi:10.1126/science.1095932.
- Murphy, F.E., Neuberger, J.W., Jacob, A.W.B., 1997. Alternatives to core–mantle boundary topography. *Phys. Earth Planet. Inter.* 145, 19–36.
- Nakagawa, T., Tackley, P.J., 2006. Three-dimensional structures and dynamics in the deep mantle: effects of post-perovskite phase change and deep mantle layering. *Geophys. Res. Lett.* 33. doi:10.1029/2006GL025719.
- Nakagawa, T., Tackley, P.J., 2008. Lateral variations in CMB heat flux and deep mantle seismic velocity caused by a thermal-chemical phase boundary in 3D spherical convection. *Earth Planet. Sci. Lett.* 271, 348–358.
- Ni, S., Helmberger, D., 2003a. Seismological constraints on the South African superplume: could be oldest distinct structure on Earth. *Earth Planet. Sci. Lett.* 206, 119–131.
- Ni, S., Helmberger, D., 2003b. Further constraints on the African superplume structure. *Phys. Earth Planet. Inter.* 140, 243–251.
- Ni, S., Tan, E., Gurnis, M., Helmberger, D., 2002. Sharp sides to the African superplume. *Science* 296, 1850–1852.
- Obayashi, M., Fukao, Y., 1997. P and PcP travel time topography for the core–mantle boundary. *J. Geophys. Res.* 102 (B8), 17825–17841.
- Oganov, A.R., Ono, S., 2004. Theoretical and experimental evidence for a post-perovskite phase of MgSiO₃ in Earth's D^{''} layer. *Nature* 430, 445–448.
- Poupinet, G., Souriau, A., Jenatton, L., 1993. A test on the Earth's core–mantle boundary structure with antipodal data: example of Fiji-Tonga earthquakes recorded in Tamanrasset, Algeria. *Geophys. J. Int.* 113 (3), 684–692.
- Revenaugh, J., Jordan, T.H., 1991. Mantle layering from ScS reverberations 4. The lower mantle and core–mantle boundary. *J. Geophys. Res.* 96 (B12), 19811–19824.
- Ricard, Y., Fleitout, L., Froidevaux, C., 1984. Geoid heights and lithospheric stresses for a dynamic Earth. *Ann. Geophys.* 2, 267–286.
- Ricard, Y., Richards, M.A., Lithgow-Bertelloni, C., Stunff, Y.L., 1993. A geodynamic model of mantle density heterogeneity. *J. Geophys. Res.* 98, 21895–21909.
- Ritsema, J., van Heijst, H.J., Woodhouse, J.H., 1999. Anomalous shear velocity structure imaged beneath Africa and Iceland. *Science* 286, 1925–1928.
- Ritsema, J., van Heijst, H.J., Woodhouse, J.H., 2004. Global transition zone tomography. *J. Geophys. Res.* 109 (B2) Art. No. B02302.
- Ritsema, J., McNamara, A.K., Bull, A.L., 2007. Tomographic filtering of geodynamical models. *J. Geophys. Res.* 112. doi:10.1029/2006JB004566 Art. No. B01303.
- Rodgers, A., Wahr, J., 1993. Inference of CMB topography from ISC PCP and PKP travel-times. *Geophys. J. Int.* 115 (3), 991–1011.
- Schubert, G., Masters, G., Olson, P., Tackley, P.J., 2004. Superplumes or plume clusters? *Phys. Earth Planet. Inter.* 146, 147–162.
- Shim, S.H., Duffy, T.S., Shen, G.Y., 2001. Stability and structure of MgSiO₃ perovskite to 2300-kilometer depth in Earth's mantle. *Science* 293, 2437–2440.
- Steinberger, B., Holme, R., 2008. Mantle flow models with core–mantle boundary constraints and chemical heterogeneities in the lowermost mantle. *J. Geophys. Res.* 113. doi:10.1029/2007JB005080 Art. No. B05403.
- Su, W.J., Dziewonski, A.M., 1997. Simultaneous inversion for 3-D variations in shear and bulk velocity in the mantle. *Phys. Earth Planet. Inter.* 100, 135–156.
- Su, W.J., Woodward, R.L., Dziewonski, A.M., 1994. Degree-12 model of shear velocity heterogeneity in the mantle. *J. Geophys. Res.* 99 (B4), 6945–6980.
- Sylvander, M., Ponce, B., Souriau, A., 1997. Seismic velocities at the core–mantle boundary inferred from P waves diffracted around the core. *Phys. Earth Planet. Inter.* 101, 189–202.
- Sze, E.K.M., van der Hilst, R.D., 2003. Core mantle boundary topography from short period PCP, PKP, and PKKP data. *Phys. Earth. Planet. Inter.* 135, 27–46.
- Tackley, P.J., 1998. Three-dimensional simulations of mantle convection with a thermo-chemical CMB boundary layer: D^{''}? In: Gurnis, M., et al. (Ed.), *The Core–Mantle Boundary Region*. American Geophysical Union, Washington, DC, pp. 231–253.
- Tackley, P.J., 2000. Mantle convection and plate tectonics: toward an integrated physical and chemical theory. *Science* 288, 2002–2007.
- Tackley, P.J., King, S.D., 2003. Testing the tracer ratio method for modeling active compositional fields in mantle convection simulations. *Geochem. Geophys. Geosys.* 4. doi:10.1029/2001GC000214.
- Tan, E., Gurnis, M., 2005. Metastable superplumes and mantle compressibility. *Geophys. Res. Lett.* 32 (20). doi:10.1029/2005GL024190.

- Tan, E., Gurnis, M., 2007. Compressible thermochemical convection and application to lower mantle structures. *J. Geophys. Res.* 112 (B6) Art. No. B06304.
- Thompson, P.F., Tackley, P.J., 1998. Generation of mega-plumes from the core–mantle boundary in a compressible mantle with temperature-dependent viscosity. *Geophys. Res. Lett.* 25 (11), 1999–2002.
- To, A., Romanowicz, B., Capdeville, Y., Takeuchi, N., 2005. 3D effects of sharp boundaries at the borders of the African and Pacific superplumes: observation and modeling. *Earth Planet. Sci. Lett.* 233, 137–153.
- Tsuchiya, T., Tsuchiya, J., Umemoto, K., Wentzcovich, R.A., 2004. Phase transition in MgSiO₃ perovskite in the Earth's lower mantle. *Earth Planet. Sci. Lett.* 224 (3–4), 241–248.
- Wang, Y., Wen, L., 2004. Mapping the geometry and geographic distribution of a very low velocity province at the base of the Earth's mantle. *J. Geophys. Res.* 109. doi:10.1029/2003JB002674.
- Yoshida, M., 2008. Core–mantle boundary topography estimated from numerical simulations of instantaneous flow. *Geochem. Geophys. Geosys.* 9 (7). doi:10.1029/2008GC002008 Art. No. Q07002.
- Zhang, S., Christensen, U., 1993. Some effects of lateral viscosity variations on geoid and surface velocities induced by density anomalies in the mantle. *Geophys. J. Int.* 114, 531–547.
- Zhong, S., Zuber, M.T., Moresi, L., Gurnis, M., 2000. Role of temperature-dependent viscosity and surface plates in spherical shell models of mantle convection. *J. Geophys. Res.* 105, 11063–11082.
- Zhong, S., Paulson, A., Wahr, J., 2003. Three-dimensional finite element modeling of Earth's viscoelastic deformation: effects of lateral variations in lithospheric thickness. *G. J. Int.* 155, 679–695.
- Zhong, S., McNamara, A.K., Tan, E., Moresi, L., Gurnis, M., 2008. A benchmark study on mantle convection in a 3-D spherical shell using CitcomS. *Geochem. Geophys. Geosys.* 9 (10). doi:10.1029/2008GC002048.